Detecting Heavy Charged Higgs Bosons
at the LHC with Four $b-$Quark Tags

D.J. Miller[1], S. Moretti[1], D.P. Roy[2,3,4], W.J. Stirling[2]

[1] *Rutherford Appleton Laboratory, Chilton, Didcot, Oxon OX11 0QX, UK*

[2] *Departments of Physics and Mathematical Sciences, University of Durham,*
South Road, Durham DH1 3LE, UK

[3] *Tata Institute of Fundamental Research, Mumbai - 400 005, India*

[4] *LAPTH, B.P. 110, F-74941 Annecy-le-Vieux Cedex, France*

Abstract

We investigate the signature of a heavy charged Higgs boson of the Minimal Super-symmetric Standard Model in the lepton plus multi-jet channel at the Large Hadron Collider with four b-tags. The signal is the gluon-gluon fusion process $gg \to t\bar{b}H^-$, followed by the $H^- \to \bar{t}b$ decay, while the main background is from $gg \to t\bar{t}b\bar{b}$. We find that the two can be separated effectively by kinematic cuts and mass reconstruction, but the signal size is not very large in the end. Nonetheless, with a good b-tagging efficiency, $\epsilon_b \sim 50\%$, this channel can provide a viable signature over a limited but interesting range of the parameter space.

1 Introduction

The detection at the Large Hadron Collider (LHC) of charged Higgs bosons would represent an unequivocal signal of physics beyond the Standard Model (SM). While the SM predicts only a neutral Higgs boson ϕ, any two Higgs doublet extension of it predicts a pair of charged Higgs bosons $H^\pm$ along with three neutral ones: the $CP-$even H and h and the $CP-$odd A [1]. This is true in particular for the Minimal Supersymmetric extension of the Standard Model (MSSM). While the SM Higgs boson may be hard to distinguish from one of the neutral Higgs bosons of the MSSM, the charged Higgs boson carries the unambiguous hallmark of the Supersymmetric (SUSY) Higgs sector. Moreover, in contrast to the case of super-particles, whose signature depends sensitively upon assumptions regarding the $R-$parity status and the nature of the SUSY breaking, the signature of $H^\pm$ bosons is fairly model independent. Therefore, there has been considerable interest in looking for SUSY signals via the associated Higgs sector and in particular the charged Higgs bosons. Furthermore, the masses and couplings of all the MSSM Higgs bosons are given at tree level in terms of only two parameters: i.e., one of the Higgs masses (e.g., M_A) and the ratio of the vacuum expectation values of the two Higgs doublets ($\tan\beta$). Thus the experimental determination of the $H^\pm$ mass $M_{H^\pm}$ would go a long way to quantitatively determining the MSSM Higgs sector.

In the MSSM one has a lower mass limit at tree level, $M_{H^\pm} > M_{W^\pm}$, which is not significantly modified by radiative corrections. There is also a comparable experimental limit from direct LEP2 searches for the charged Higgs boson [2]. In fact, using the MSSM mass relations one can get a strong indirect bound on $M_{H^\pm}$ in the low $\tan\beta$ region from the LEP2 limit on M_h, the mass of the lightest Higgs boson of the MSSM [3]. As shown in [4], however, this constraint can be evaded in modest extensions of the MSSM involving an additional singlet Higgs boson. Therefore it does not preclude direct searches for charged Higgs bosons in the low $\tan\beta$ region.

The Tevatron and (especially) LHC hadron colliders offer the possibility to carry on the charged Higgs boson search to higher masses because of their higher energy reach. Here, the most prominent source of $H^\pm$ production for $M_{H^\pm} < m_t$ (light charged Higgs boson) is top quark decay, $t \to bH^+$. The corresponding branching ratio (BR) can easily be estimated from the relevant part of the MSSM Lagrangian

$$\mathcal{L} = \frac{e}{\sqrt{2}M_{W^\pm}\sin\theta_W}H^+(m_b\tan\beta\ \bar{t}b_R + m_t\cot\beta\ \bar{t}b_L), \tag{1}$$

written in the diagonal CKM matrix approximation. It suggests a large $\bar{t}bH^+$ Yukawa coupling and hence large branching fraction for the $t \to bH^+$ decay in the regions of low as well as very high $\tan\beta$, i.e.,

$$\tan\beta \lesssim 1 \quad \text{and} \quad \tan\beta \gtrsim m_t/m_b. \tag{2}$$

Interestingly, these two regions are favoured by $b - \tau$ unification for a related reason: i.e., assuming $m_b = m_\tau$ at the GUT scale one needs a large $\bar{t}bH^+$ Yukawa coupling contribution to the Renormalisation Group Equations (RGEs) to control the rise of m_b at low energy scales [5]. The dominant decay channels of light charged Higgs bosons are $H^+ \to c\bar{s}$ and $H^+ \to t^*\bar{b} \to b\bar{b}W$ at $\tan\beta \lesssim 1$, while the $H^+ \to \tau^+\nu_\tau$ decay dominates for $\tan\beta > 1$ [6]. It may be noted here that there are already some modest limits on $M_{H^\pm}$ from the Tevatron top quark data [7] in the two regions (2). The search can be extended over a wider region of $M_{H^\pm}$ and $\tan\beta$ at the forthcoming Tevatron upgrade (TeV-2), by exploiting the distinctive τ polarization in $H^\pm$ decay [8, 9]. Moreover the detection range can be enlarged to encompass practically the entire $M_{H^\pm} < m_t$ region at the LHC [9, 10].

We shall investigate here the prospect of charged Higgs searches at the LHC in the opposite case, when $M_{H^\pm} > m_t$ (heavy charged Higgs boson). The dominant decay mode of such a particle is $H^\pm \to t\bar{b}$, which suffers from a large QCD background. Therefore, it is not surprising that detecting a charged Higgs boson heavier than top has been generally regarded as very hard[1]. The largest signal cross sections at the LHC are expected to come from the associated production of $H^\pm$ with top (anti)quarks, followed by its dominant decay mode, i.e.,

$$gb \to tH^- \to t\bar{t}b, \tag{3}$$

and

$$gg \to t\bar{b}H^- \to t\bar{t}b\bar{b}. \tag{4}$$

After the decay of the top pair one expects 4 $b-$jets in (4) and 3 in (3), where the accompanying $\bar{b}$ sea-quark does not take part in the hard scattering and hence escapes detection by being produced close to the beam direction. The charged Higgs signal from (3) and (4) were investigated in [14] and [15], respectively, assuming triple b-tagging. The dominant (QCD) background processes in either case are

$$gg \to t\bar{t}b\bar{b}, \tag{5}$$

$$gg \to t\bar{t}gg \ + \ t\bar{t}q\bar{q}, \tag{6}$$

with one or more of the light parton jets in the latter process misidentified as b. Both the analyses found fairly viable $H^\pm$ signals in the two above mentioned regions of $\tan\beta$, corresponding to a large $H^+\bar{t}b$ Yukawa coupling. Recently the associated production of charged Higgs and $W^\pm$ bosons has been investigated in [16]. Being a second order electroweak process, however, the size of the resulting signal is smaller than those of reactions

---

[1]Recent new insights into the problem can be found in Ref. [11], where the exploitation of top quark polarisation effects was advocated. For an alternative approach, using the much suppressed but somewhat cleaner $H^\pm \to \tau\nu$ decay channel, see Ref. [12]. In the same spirit, the mode $H^\pm \to W^\pm h$ is currently being investigated in Ref. [13].

(3)–(4). Furthermore, it suffers from an overwhelming irreducible background induced by top-antitop production and decay [17]. Therefore it does not seem to offer a useful $H^\pm$ signal at the LHC. Similarly, the production of charged Higgs scalars in association with b quarks [18] is burdened by a large combinatorial background as well as a formidable multi-jet QCD noise.

We shall present here an analysis of $H^\pm$ signals at the LHC produced via the gluon-gluon fusion process (4)[2], assuming all four $b-$quark jets to be tagged. Of course the size of this signal will be smaller than in the 3b-tagged channel. However, we have verified, while computing the gg-initiated process, that, by imposing a transverse momentum cut of 20 to 30 GeV on the spectator $b-$jet in reaction (4), the typical loss of signal is not dramatic: e.g., about a factor of 2 to 3, for $M_{H^\pm} \approx 300$ GeV. Besides, it is clear from the analyses in Refs. [14, 15] that the background (6) with double b-mis-tagging will be very small. Indeed, we have explicitly confirmed this by recomputing the processes (5)–(6) from scratch. The same conclusion applies to the the case of single b-mis-tagging in events of the type:

$$gb \to t\bar{t}gb. \tag{7}$$

Therefore we only need to worry about the $t\bar{t}b\bar{b}$ background (5). Moreover, we shall see below that the kinematics of the pair of $b-$jets accompanying the $t\bar{t}$ pair is expected to be rather different for the background, as compared to the signal (4). Consequently such a background can be suppressed effectively by using suitable kinematic cuts on these $b-$jets. As a result, we find a cleaner (but smaller) charged Higgs boson signal in the 4b-tagged channel than in the 3b-ones considered in [14, 15]. In the following Section we present the main steps in the calculation of the signal and background cross sections. The event selection strategy and choice of kinematic cuts are outlined in Section 3. The quantitative discussion of our analysis is presented in Section 4. Finally, we summarise the main results and present our conclusions in Section 5.

2 Calculation of signal and background cross sections

The relatively large number of Feynman diagrams involved in the signal process, $gg \to t\bar{b}H^-$ (4), renders the algebraic expressions for the corresponding 'squared' matrix element rather long and cumbersome. This drawback of the trace method can be obviated by resorting to helicity amplitude techniques, which allow one to write down the 'complex' amplitudes in more compact form. In expressing the helicity amplitudes we have made use of the formalism described, e.g., in Ref. [20], to which we refer the reader for technical details. Here, we briefly outline the procedure and give all the formulae needed to implement our calculations in a numerical program, as they have not appeared in the literature previously.

---

[2]For some early numerical studies of the on-shell $2 \to 3$ production, see Ref. [19].

$\lambda_1\lambda_2$	$Y(p_1, \lambda_1; p_2, \lambda_2; c_R, c_L)$
$++$	$c_R\mu_1\eta_2 + c_L\mu_2\eta_1$
$+-$	$c_L S(+, p_1, p_2)$

Table 1: The Y functions for the two independent helicity combinations in terms of the functions S, η and μ defined in the text. The remaining Y functions can be obtained by flipping the sign of the helicities and exchanging $+$ with $-$ in the S functions and R with L in the chiral coefficients.

First, one needs to introduce some spinor functions, Y and Z [21, 22, 23], given in Tabs. 1–2, which can be defined in terms of the following quantities ($\epsilon^{0123} = 1$ is the Levi-Civita tensor):

$$S(+, p_1, p_2) = 2\frac{(p_1 \cdot k_0)(p_2 \cdot k_1) - (p_1 \cdot k_1)(p_2 \cdot k_0) + i\epsilon_{\mu\nu\rho\sigma}k_0^\mu k_1^\nu p_1^\rho p_2^\sigma}{\eta_1\eta_2}, \tag{8}$$

$$S(-, p_1, p_2) = S(+, p_2, p_1)^*,$$

$$\mu_i = \pm\frac{m_i}{\eta_i}, \qquad \eta_i = \sqrt{2(p_i \cdot k_0)}, \tag{9}$$

where p_i and m_i represent the four-momentum and mass of the particle i (for which $p_i^2 = m_i^2$) and k_0 and k_1 are two arbitrary four-vectors such that

$$k_0 \cdot k_0 = 0, \qquad k_1 \cdot k_1 = -1, \qquad k_0 \cdot k_1 = 0. \tag{10}$$

In the first of the two expressions in eq. (9) the signs $+$ and $-$ refer to particles and to antiparticles, respectively.

In Tabs. 1 and 2 the (chiral) coefficients c_R and c_L are those entering the fundamental fermion-fermion-boson vertices, described through the expressions

$$\Gamma^{(')\mu} = \gamma^\mu\Gamma^{(')}, \tag{11}$$

and

$$\Gamma^{(')} = c_R^{(')}P_R + c_L^{(')}P_L, \tag{12}$$

with

$$P_R = \frac{1 + \gamma_5}{2}, \qquad P_L = \frac{1 - \gamma_5}{2}, \tag{13}$$

the chiral projectors.

If we make the following assignments for the momenta p_i (with $i = 1, ...5$), which we assume incoming in the initial state and outgoing in the final state, and helicities λ_i (with $i = 1, ...4$) of the external particles in the $2 \to 3$ reaction

$$g(p_1, \lambda_1) + g(p_2, \lambda_2) \to t(p_3, \lambda_3) + \bar{b}(p_4, \lambda_4) + H^-(p_5), \tag{14}$$

4

$\lambda_1\lambda_2\lambda_3\lambda_4$	$Z(p_1,\lambda_1;p_2,\lambda_2;p_3,\lambda_3;p_4,\lambda_4;c_R,c_L;c_R',c_L')$
$++++$	$-2[S(+,p_3,p_1)S(-,p_4,p_2)c_R'c_R - \mu_1\mu_2\eta_3\eta_4 c_R'c_L - \eta_1\eta_2\mu_3\mu_4 c_L'c_R]$
$+++-$	$-2\eta_2 c_R[S(+,p_4,p_1)\mu_3 c_L' - S(+,p_3,p_1)\mu_4 c_R']$
$++-+$	$-2\eta_1 c_R[S(-,p_2,p_3)\mu_4 c_L' - S(-,p_2,p_4)\mu_3 c_R']$
$+-++$	$-2\eta_4 c_R'[S(+,p_3,p_1)\mu_2 c_R - S(+,p_3,p_2)\mu_1 c_L]$
$++--$	$-2[S(+,p_1,p_4)S(-,p_2,p_3)c_L'c_R - \mu_1\mu_2\eta_3\eta_4 c_L'c_L - \eta_1\eta_2\mu_3\mu_4 c_R'c_R]$
$+-+-$	0
$+--+$	$-2[\mu_1\mu_4\eta_2\eta_3 c_L'c_L + \mu_2\mu_3\eta_1\eta_4 c_R'c_R - \mu_2\mu_4\eta_1\eta_3 c_L'c_R - \mu_1\mu_3\eta_2\eta_4 c_R'c_L]$
$+---$	$-2\eta_3 c_L'[S(+,p_2,p_4)\mu_1 c_L - S(+,p_1,p_4)\mu_2 c_R]$

Table 2: The Z functions for all independent helicity combinations in terms of the functions S, η and μ defined in the text. The remaining Z functions can be obtained by flipping the sign of the helicities and exchanging $+$ with $-$ in the S functions and R with L in the chiral coefficients.

so that $p_1^2 \equiv p_2^2 = 0$, $p_3^2 = m_t^2$ (with $\Gamma_3 = \Gamma_t \neq 0$), $p_4^2 = m_b^2$ (with $\Gamma_4 = \Gamma_b = 0$) and $p_5^2 = M_{H^\pm}^2$, then the Feynman amplitudes $T_i^{\{\lambda\}}$ can be written (apart from a phase, a factor $g_s^2 e$ and neglecting the colour matrices) as (here and below, $\{\lambda\}$ refers cumulatively to the helicities of the external particles λ_i with $i = 1,...4$, and $\sum_{\{\lambda\}}$ to the summation over all their possible combinations)

$$T_1^{\{\lambda\}} = \quad\quad\quad\quad = \tag{15}$$

$$+ \; N_1 N_2 D_4(p_3+p_5)D_4(p_2-p_4) \sum_{i=1,2,4}\sum_{j=2,4} b_i b_j \sum_{\lambda=\pm}\sum_{\lambda'=\pm}$$
$$Y(p_3,\lambda_3;p_i,\lambda;c_R^H,c_L^H)$$
$$\times \; Z(p_i,\lambda;p_j,\lambda';p_1,\lambda_1;q_1,\lambda_1;c_R^g,c_L^g;1,1)$$
$$\times \; Z(p_j,\lambda';p_4,-\lambda_4;p_2,\lambda_2;q_2,\lambda_2;c_R^g,c_L^g;1,1),$$

$$T_2^{\{\lambda\}} = \quad\quad\quad\quad = \tag{16}$$

$$
\begin{aligned}
- \quad & N_1 N_2 D_3(p_3 - p_1) D_4(p_2 - p_4) \sum_{i=1,3} \sum_{j=2,4} b_i b_j \sum_{\lambda=\pm} \sum_{\lambda'=\pm} \\
& Z(p_3, \lambda_3; p_i, \lambda; p_1, \lambda_1; q_1, \lambda_1; c_R^g, c_L^g; 1, 1) \\
\times \quad & Y(p_i, \lambda; p_j, \lambda'; c_R^H, c_L^H) \\
\times \quad & Z(p_j, \lambda'; p_4, -\lambda_4; p_2, \lambda_2; q_2, \lambda_2; c_R^g, c_L^g; 1, 1),
\end{aligned}
$$

$$
T_3^{\{\lambda\}} \quad = \quad \text{(diagram)} \quad = \tag{17}
$$

$$
\begin{aligned}
+ \quad & N_1 N_2 D_3(p_3 - p_1) D_3(p_4 + p_5) \sum_{i=1,3} \sum_{j=1,2,3} b_i b_j \sum_{\lambda=\pm} \sum_{\lambda'=\pm} \\
& Z(p_3, \lambda_3; p_i, \lambda; p_1, \lambda_1; q_1, \lambda_1; c_R^g, c_L^g; 1, 1) \\
\times \quad & Z(p_i, \lambda; p_j, \lambda'; p_2, \lambda_2; q_2, \lambda_2; c_R^g, c_L^g; 1, 1) \\
\times \quad & Y(p_j, \lambda'; p_4, -\lambda_4; c_R^H, c_L^H),
\end{aligned}
$$

$$
T_4^{\{\lambda\}} \quad = \quad \text{(diagram)} \quad = \quad T_1^{\{\lambda\}}(1 \leftrightarrow 2), \tag{18}
$$

$$
T_5^{\{\lambda\}} \quad = \quad \text{(diagram)} \quad = \quad T_2^{\{\lambda\}}(1 \leftrightarrow 2), \tag{19}
$$

$$
T_6^{\{\lambda\}} \quad = \quad \text{(diagram)} \quad = \quad T_3^{\{\lambda\}}(1 \leftrightarrow 2), \tag{20}
$$

6

$$T_7^{\{\lambda\}} \;=\; \text{} \;=$$ (21)

$$
\begin{aligned}
+ \;\; & N_1 N_2 D_4(p_3 + p_5) D(p_1 + p_2) \sum_{i=1,2,4} b_i \sum_{\lambda=\pm} \sum_{\lambda'=\pm} \\
& Y(p_3, \lambda_3; p_i, \lambda; c_R^H, c_L^H) \\
\times \;\; & [Y(p_i, \lambda; p_1, \lambda'; 1, 1) Y(p_1, \lambda'; p_4, -\lambda_4; c_R^g, c_L^g) \\
& \times Z(p_1, \lambda_1; q_1, \lambda_1; p_2, \lambda_2; q_2, \lambda_2; 1, 1; 1, 1) \\
& + 2\, Z(p_2, \lambda_2, q_2, \lambda_2; p_i, \lambda; p_4, -\lambda_4; 1, 1; c_R^g, c_L^g) \\
& \times Y(p_1, \lambda_1; p_2; \lambda'; 1, 1) Y(p_2, \lambda'; q_1, \lambda_1; 1, 1) \\
& - \operatorname{same}(1 \leftrightarrow 2)],
\end{aligned}
$$

$$T_8^{\{\lambda\}} \;=\; \text{} \;=$$ (22)

$$
\begin{aligned}
- \;\; & N_1 N_2 D_3(p_4 + p_5) D(p_1 + p_2) \sum_{i=1,2,3} b_i \sum_{\lambda=\pm} \sum_{\lambda'=\pm} \\
& [Y(p_3, \lambda_3; p_1; \lambda'; 1, 1) Y(p_1, \lambda'; p_i, \lambda; c_R^g, c_L^g) \\
& \times Z(p_1, \lambda_1; q_1, \lambda_1; p_2, \lambda_2; q_2, \lambda_2; 1, 1; 1, 1) \\
& + 2\, Z(p_2, \lambda_2, q_2, \lambda_2; p_3, \lambda_3; p_i, \lambda; 1, 1; c_R^g, c_L^g) \\
& \times Y(p_1, \lambda_1; p_2; \lambda'; 1, 1) Y(p_2, \lambda'; q_1, \lambda_1; 1, 1) \\
& - \operatorname{same}(1 \leftrightarrow 2)] \\
\times \;\; & Y(p_i, \lambda; p_4, -\lambda_4; c_R^H, c_L^H),
\end{aligned}
$$

where we have introduced the coefficients $b_1 = b_2 = -b_3 = -b_4 = 1$, to distinguish incoming and outgoing particles, and the propagators $D_i(p) = 1/(p^2 - m_i^2 + i m_i \gamma_i)$ (with $\gamma_i \equiv \Gamma_i$ if $p^2 > 0$ and $\gamma_i = 0$ otherwise[3]) and $D(p) = 1/p^2$. In eqs. (15)–(22), q_i (with $i = 1, 2$) is an arbitrary four-momentum not parallel to p_i (i.e., $q_i \neq \alpha p_i$ with α constant) and $N_i = [4(q_i \cdot p_i)]^{-1/2}$; see Ref. [20] for more details.

---

[3]That is, we include a finite quark width only in resonant propagators.

The coefficients c_R and c_L for the vertices relevant to such a process are

$$(c_R^H, c_L^H) = -\frac{1}{\sqrt{2}M_{W^{\pm}}\sin\theta_W}(m_b\tan\beta, m_t\cot\beta) \tag{23}$$

for the charged Higgs, see eq. (1), and simply

$$(c_R^g, c_L^g) = (1,1) \tag{24}$$

for the gluon to quarks couplings. As usual, θ_W represents the Weinberg angle. Here, the bottom and top quark masses entering the Yukawa interaction are those defined at the propagator pole, i.e., $m_{b,t} \equiv \bar{m}_{b,t}(m_{b,t})$, where $\bar{m}_{b,t}(Q)$ are the running masses at the (energy) scale Q (see below). Also note that in eqs. (23)–(24) we have factored out the overall couplings $-ie$ and $-ig_s$ of the Lagrangian.

As for the colour structure of our process, one should notice that in this case there are two basic combinations of colour matrices associated with the Feynman graphs (15)–(22), that is $(t^A t^B)_{i_3 i_4}$ and $(t^B t^A)_{i_3 i_4}$, where $A(i_3)$ and $B(i_4)$ identify the colours of the gluons(quarks) 1(3) and 2(4), respectively. In fact, it should be recalled that the colour terms associated with the triple-gluon vertices are nothing but the structure constants f^{ABX} of the $SU(N_C)$ gauge group, for which

$$[t^A, t^B]_{i_3 i_4} \equiv (t^A t^B)_{i_3 i_4} - (t^B t^A)_{i_3 i_4} = \mathrm{i}f^{ABX}t^X_{i_3 i_4}, \tag{25}$$

X being in our case the colour label of the virtual gluon. Therefore, one can conveniently group the original eight Feynman amplitudes as follows

$$M_+^{\{\lambda\}} = \sum_{i=1}^{3} T_i^{\{\lambda\}} + \sum_{i=7}^{8} T_i^{\{\lambda\}} \tag{26}$$

$$M_-^{\{\lambda\}} = \sum_{i=4}^{6} T_i^{\{\lambda\}} - \sum_{i=7}^{8} T_i^{\{\lambda\}}.$$

The standard form of the matrix element (ME) squared, summed/averaged over the final/initial spins and colours, is then

$$|\mathcal{M}|^2(gg \to t\bar{b}H^-) = \frac{g_s^4 e^2}{256} \sum_{\{\lambda\}} \sum_{i,j=\pm} M_i^{\{\lambda\}} M_j^{\{\lambda\}*} C_{ij}, \tag{27}$$

where C_{ij} is a 2×2 colour matrix with elements

$$C_{++} \equiv C_{--} = \frac{N_C}{4}(N_C^2 - 2 + \frac{1}{N_C^2}) \tag{28}$$

$$C_{+-} \equiv C_{-+} = \frac{N_C}{4}(\frac{1}{N_C^2} - 1),$$

$N_C = 3$ being the number of colours in QCD. Finally, notice that the ME for the charge conjugated process

$$g(p_1, \lambda_1) + g(p_2, \lambda_2) \rightarrow b(p_3, \lambda_3) + \bar{t}(p_4, \lambda_4) + H^+(p_5), \qquad (29)$$

now with $p_3^2 = m_b^2$ and $p_4^2 = m_t^2$ (and, correspondingly, $\Gamma_3 = 0$ and $\Gamma_4 = \Gamma_t$), can be obtained by the simple replacement $c_R^H \leftrightarrow c_L^H$.

The above formulae refer to the $2 \rightarrow 3$ process of on-shell $H^{\pm}-$ and $t-$production. In reality, both these particles eventually decay inside the detectors, so that one ought also to consider their decay signatures. We have included these decays by convoluting the $2 \rightarrow 3$ (unpolarised) production ME with the $3-$ and $4-$body decay MEs of top and Higgs, respectively, which are well known and can be found in the literature. In doing so, we introduce several simplifications[4]. Firstly, we neglect spin effects in the top decays. Secondly, we do not consider interference effects between diagrams involving H^+ and H^- production. Thirdly, Fermi-Dirac interferences due to indistinguishibility of $b-$quarks (or, equivalently, of $\bar{b}-$antiquarks) in the final state are not included. However, while noticeably simplifying the numerical evaluation, we have checked that these approximations do not spoil the validity of our analysis. In fact, we have also produced the exact $2 \rightarrow 8$ ME for the signal process, including all the above spin and interference effects, by means of the `HELAS` [24] subroutines and the MadGraph [25] package, and compared its yield to that of the simplified implementation. We have always found a good agreement between the two, with residual effects surviving only in differential spectra which are of no concern in our analysis. Indeed, for the typical quantities we shall investigate (transverse momenta, pseudorapidity, multi-jet invariant masses, etc.), the results generally coincide within numerical accuracy.

The `HELAS` libraries and MadGraph have also been used to generate the background process (5a), as any analytical expression for the latter would be much too cumbersome. Indeed, thirty-six different Feynman diagrams are involved (actually twice that if one considers also those induced by the above mentioned Fermi-Dirac statistics), with ten external particles.

Both signal and background MEs have been integrated by means of `VEGAS` [26], with a careful mapping of the phase space, to account for the various resonances. In some cases, where the multi-dimensional integrations (21 in total, for the $2 \rightarrow 8$ implementation) are more problematic, the `VEGAS` results have been cross-checked against those obtained by using `RAMBO` [27] as well as the `D01GCF` and `D01GZF` NAGLIB subroutines.

In addition to the phase space integration, one also has to convolute in the (x, Q^2)-dependent Parton Distribution Functions (PDFs) for the the two incoming gluons. These have been evaluated at leading-order, by means of the packages MRS-LO(05A,09A,10A,01A,07A) [28]. The Q^2 used for the latter was the CM energy (squared)

---

[4]Note that in the numerical simulations we allow the top quark and Higgs bosons to be 'off-shell', that is, $p_{3[4]}^2 \neq m_t^2$ and $p_5^2 \neq M_{H^\pm}^2$ in the above formulae for process (14)[(29)].

at the parton level, i.e., $\hat{s} = x_1 x_2 s$, with $\sqrt{s} = 14$ TeV taken as the CM energy for the LHC. The same choice has been adopted for the scale of the strong coupling constant α_s, evaluated again at lowest order, with $\Lambda_{\mathrm{QCD}}^{N_f=4}$ chosen in accordance with that of the PDF set used.

In addition, notice that before the signal and background cross sections can be computed reliably, one must take into account the effects of higher-order QCD corrections to the tree-level processes (see the discussion in Ref. [15]). The full next-to-leading order corrections are as yet unknown for the processes we consider. For the case of the Higgs signal, the dominant effects can however by mimicked by adopting the pole masses in the Higgs-fermion coupling entering the production process, see eq. (23), rather than the running ones [29]. As for the $t\bar{t}b\bar{b}$ background, we estimate their effect by including an overall K-factor of 1.5 throughout this study [15].

The numerical values of the SM parameters are (pole masses are assumed):

$$m_\ell = m_{\nu_\ell} = m_u = m_d = m_s = m_c = 0,$$

$$m_b = 4.25 \text{ GeV}, \qquad m_t = 175 \text{ GeV},$$

$$M_Z = 91.19 \text{ GeV}, \qquad \Gamma_Z = 2.5 \text{ GeV},$$

$$M_{W^\pm} = 80.23 \text{ GeV}, \qquad \Gamma_W = 2.08 \text{ GeV}. \tag{30}$$

For the top width Γ_t, we have used the LO value calculated within the MSSM (i.e., $\Gamma_t = 1.55$ GeV for $M_{H^\pm} \gg m_t$). Furthermore, we have adopted M_A and $\tan\beta$ as independent input parameters defining the Higgs sector of the MSSM at LO. The charged Higgs width $\Gamma_{H^\pm}$ has been computed by means of the program HDECAY, which indeed requires M_A, rather than $M_{H^\pm}$, as mass input [30] (the masses of the super-partners of the ordinary matter particles were fixed well above 1 TeV, so they enter neither the top nor the charged Higgs decay chain as real objects and render the virtual SUSY corrections to the $H^\pm tb$ vertex negligible [31]). As this program uses running quark masses (in the modified Minimal Subtraction scheme) in evaluating the decay width of the $H^\pm \to tb$ channel we have, for consistency, used running values for all such quantities in the $H^\pm tb$ couplings entering our decay MEs for the signal (but not in the propagators and in the phase space, for which the pole masses $m_b \equiv \bar{m}_b(m_b)$ and $m_t \equiv \bar{m}_t(m_t)$ of eq. (30) have been used).

Finally, notice that we stop our analyses at the parton level, without considering fragmentation and hadronisation effects. Thus, jets are identified with the partons from which they originate and all cuts are applied directly to the latter. In particular, when selecting $b-$jets, a vertex tagging is implied, with finite efficiency ϵ_b per tag. As four $b-$jets will be required to be tagged, the overall efficiency will be ϵ_b^4, by which both signal and background rates will eventually have to be multiplied. For simplicity, we assume no correlations between the four tags, nor do we include mis-identification of light-quark (including $c-$quark) jets produced in the $W^\pm$ decay as $b-$jets.

3 Selection strategy

In this Section we describe the kinematic procedure adopted to disentangle charged Higgs events (4) from the background (5) in the $t\bar{t}b\bar{b}$ channel. First, one of the top quarks is required to decay leptonically ($t \to b\ell\nu$) to provide a hard lepton ($\ell = e, \mu$) trigger and avoid the QCD background, while the other decays hadronically ($\bar{t} \to \bar{b}qq'$), with ($q, q' \neq b, t$). The resulting branching fraction is $2 \times 2/9 \times 2/3$, with the factor of two accounting for the fact that each of the $W^{\pm}$'s can decay either leptonically or hadronically. We assume that the charge of the $b-$jet is not measured. Thus, the signature we are discussing is effectively

$$4b \ + \ 2 \text{ jets} \ + \ \ell^{\pm} \ + \ p_{\text{miss}}^T, \tag{31}$$

where the 2 un-tagged jets and the $\ell + p_{\text{miss}}^T (= p_\nu^T)$ arise from the $W^+ W^-$ boson pair produced in the $t\bar{t}$ decay.

We note that all the decay products of the top quarks in the signal are expected to be hard while one of the accompanying $b-$quarks (or both depending on the $M_{H^\pm} - m_t$ mass difference) could be soft. Therefore we impose a relatively demanding transverse momentum cut on the two softer $b-$jets,

$$p_{b_1,b_2}^T > 20 \text{ GeV}. \tag{32}$$

For simplicity, we do the same for the rest, i.e.,

$$p_{\ell^\pm,\nu,j,b_3,b_4}^T > 20 \text{ GeV}. \tag{33}$$

However, we will present some results also for the case of a 30 GeV cut in transverse momentum (on both jets and leptons), since the latter threshold is believed optimal in increasing the b-tagging efficiency at high luminosity (this is needed in order to render the $4b$-signal of a charged Higgs boson statistically significant): see Ref. [32]. Furthermore, we require the pseudorapidity of jets and leptons to be

$$|\eta_{b,j,\ell^\pm}| < 2.5, \tag{34}$$

and allow for their detection as separate objects by imposing the following isolation criteria:

$$\Delta R_{bb,bj,jj,b\ell^\pm,j\ell^\pm} > 0.4, \tag{35}$$

by means of the variable

$$\Delta R_{ij} = \sqrt{(\Delta\eta_{ij})^2 + (\Delta\phi_{ij})^2}, \tag{36}$$

defined in terms of relative differences in pseudorapidity η_{ij} and azimuth ϕ_{ij}, with $i \neq j = j, b, \ell^\pm$.

We simulate calorimeter resolution by a Gaussian smearing of p^T (without shower spreading and with uniform pseudorapidity/azimuth segmentation), with $(\sigma(p^T)/p^T)^2 =$

$(0.6/\sqrt{p^T})^2 + (0.04)^2$ for all the jets and $(\sigma(p^T)/p^T)^2 = (0.12/\sqrt{p^T})^2 + (0.01)^2$ for the leptons [14]. The corresponding p^T_{miss} is evaluated from the vector sum of the jet and lepton transverse momenta after resolution smearing.

To improve the signal/background ratio and to estimate the $H^\pm$ mass we follow a strategy similar to the one in Ref. [14].

(a) The invariant mass of the two un-tagged jets is required to be consistent with $M_{W^\pm}$,

$$|M_{jj} - M_{W^\pm}| \leq 15 \text{ GeV}. \tag{37}$$

(b) The neutrino momentum is reconstructed by equating $p^T_\nu = p^T_{\mathrm{miss}}$ and fixing the longitudinal component p^L_ν via the invariant mass constraint $M(\ell\nu) = M_{W^\pm}$. The latter gives two solutions. If they are complex we discard the imaginary parts and they coalesce; otherwise both the solutions are retained.

(c) The invariant mass formed by combining the un-tagged jet pair with one of the four $b-$jets is required to match m_t,

$$|M_{jjb} - m_t| \leq 25 \text{ GeV}. \tag{38}$$

If several $b-$jets satisfy this constraint, the one giving the best agreement with m_t is selected.

(d) The invariant mass formed by combining ℓ and ν with one of the 3 remaining $b-$jets is also required to match m_t within ± 25 GeV. If several $b-$jets satisfy this, the one giving the best agreement with m_t is selected along with the corresponding value of p^L_ν.

(e) The remaining pair of $b-$jets may be looked upon as the $b\bar{b}$ pair accompanying the $t\bar{t}$ in the signal (4) and background (5). Note that one of these $b-$jets is expected to come from the $H^\pm$ decay in the signal, while for the background they both come from a gluon splitting. Consequently, in the latter case one supposes the $b\bar{b}$ pair to have a smaller invariant mass. Furthermore, one may also expect the energy and the relative angle of the two b's to be rather different, between signal and background. We compare the signal and background cross sections against M_{bb}, E_{b_1}, E_{b_2} (with the labels 1[2] referring to the more[less] energetic of the two $b-$quarks) and $\cos\theta_{bb}$ and suppress the latter by suitable cuts in one or more such quantities.

(f) Finally we combine each of the reconstructed $t-$quarks with each of the remaining $b-$jets to obtain 4 entries for the bt invariant mass M_{bt}. For each signal point, one of these entries will correspond to the parent $H^\pm$ mass while the other three will represent the combinatorial background. We plot the signal and background cross

12

sections against this quantity. The former will show the resonant peak at $M_{H^\pm}$ sitting on top of a broad combinatorial background, while the latter will show only a broad distribution in M_{bt}. As we shall see below, the Breit-Wigner peak itself can help to improve the signal/background ratio further as well as to determine the $H^\pm$ mass.

(g) For $M_{H^\pm} \gg m_t$, one of the above mentioned $b-$jets (i.e., the one coming from the $H^+ \to t\bar{b}$ decay) would generally be much harder than the other. In this case, one can expect to reduce the combinatorial background by combining each of the top quark pair with the harder of the two accompanying $b-$jets. This would give two values of invariant mass M_{bt} for each signal point, one of which corresponds to the parent $H^\pm$ mass. Therefore we shall also show the signal and background cross sections against this quantity for $M_{H^\pm} \geq 300$ GeV.

4 Results and discussion

Both signal (4) and background (5) cross sections are finite over the entire phase space, provided the $b-$quark mass is retained in the calculation. Thus, as a preliminary exercise, we look at the total production rates of the above processes with no cuts whatsoever, as they would appear in the decay channel (31) to an ideal detector. This is done in the top plot of Fig. 1. Here, the rates have been obtained by multiplying the $2 \to 3$ cross section times the relevant BRs of top and Higgs decays, thus neglecting finite width effects. The signal rates depend on both $M_{H^\pm}$ and $\tan\beta$, and so they are plotted as a function of the former for two values of the latter in the favourable regions (2). In contrast, the background rates are independent of both and are indicated by the arrow next to the $y-$axis. The insert in the top plot of Fig. 1 enlarges the region around the threshold region $M_{H^\pm} \approx m_t$, where the $\mathrm{BR}(H^+ \to t\bar{b})$ increases rapidly. A striking feature of the production cross sections is the apparently poor signal-to-background ratio, over all the $M_{H^\pm}$ spectrum considered, irrespective of $\tan\beta$. Note however that no dedicated treatment of the final state kinematics has yet been performed. Indeed, the number of heavy charged Higgs events produced is sizable up to around 800 GeV, where the total cross section at both $\tan\beta$ values is still around several femtobarns. At its maximum, just after the opening of the $H^+ \to t\bar{b}$ decay threshold, it can be larger by about two orders of magnitude.

Fig. 1 has been produced by using the MRS-LO(05A) PDF set. In Tab. 3 we study the dependence of both signal and background rates on the choice of the structure functions, using the other four fits of the 1998 Martin-Roberts-Stirling-Thorne LO package[5]. For reference, we have used the value $\tan\beta = 30$, whereas five different choices of Higgs masses in the heavy range have been adopted. Differences in the signal cross sections are found

---

[5]The additional fits correspond to varying the large-x gluon and α_s about their central preferred values.

to be within the $\pm 25\%$ range, with a somewhat smaller range for the background. Furthermore, changing the renormalisation (Q) and factorisation (μ) scales from their common default value $\sqrt{\hat{s}}$ to, e.g., the sum of the rest masses in the $2 \to 3$ and $2 \to 4$ production process (4) and (5), induces variations in the results of the same order as above. As a consequence, an overall error of, say, approximately 30–35% should be taken as an estimate of the uncertainties related to the PDFs and α_s throughout the paper.

As the next step of our analysis, we implement the acceptance cuts (32)–(35) and the selection cuts described through steps (a)–(d) in the previous Section. The total signal and background cross sections after such constraints have been enforced can be found in the bottom plot of Fig. 1. Note that the kinematic procedure outlined above has been helpful in increasing the signal-to-background ratio over all the Higgs mass spectrum (compare to the curves above). The signal rates have been depleted too, mainly by the $p_{b_2}^T$ cut (32), dropping to a few femtobarns for values of $\tan\beta$ at the upper and lower end of the parameter range and Higgs masses below 700 GeV or so. For intermediate values of $\tan\beta$, e.g., around the minimum of the production cross section occurring at $\tan\beta \approx 7$, prospects are more gloomy. In fact, the signal rates are always below 1 fb or so in this case, for any $M_{H^\pm}$ value. Furthermore, as here (and in the following as well) we have retained a finite value for Γ_H, the reader may appreciate – by comparing this plot to the one above – the suppressing(enhancing) effects of a larger(smaller) Higgs width at low(high) $M_{H^\pm}$ values for $\tan\beta = 40$, with respect to the case $\tan\beta = 1.5$ (the effects of a $\Gamma_t \neq 0$ are the same in all cases). As intimated in the previous Section, we also have considered the case of a 30 GeV cut in all transverse momenta (including the missing one). The insert in the bottom plot of Fig. 1 presents the consequent suppression on the signal rates for, e.g., $\tan\beta = 40$. Far from the $M_{H^\pm} \approx m_t + m_b$ threshold, the ratio between the two cross sections stabilises at just below three (irrespectively of $\tan\beta$). For the background, the reduction is slightly higher, a factor of four or so.

Continuing with step (e) of our plan, we next investigate the mass, angular and energy behaviours of the two $b-$quarks accompanying the $t\bar{t}$ pair, after the acceptance and selection cuts have been implemented. The relevant plots can be found in Fig. 2. For reference, the value chosen for $\tan\beta$ is 40, whereas for the charged Higgs masses we have taken $M_{H^\pm} = 214(310)[407]\{506\}$ GeV, corresponding to $M_A = 200(300)[400]\{500\}$ GeV. (Spectra look rather similar if a $p_{\ell^\pm,\nu,\text{j}}^T, b > 30$ GeV cut is enforced instead.) As already foreseen, one can appreciate significant differences in all four quantities considered, as long as $M_{H^\pm}$ is well above m_t. If $M_{H^\pm}$ is not much larger than 200 GeV, the signal and background distributions are similar except for the angular variable. In contrast, if $M_{H^\pm} \geq 300$ GeV, one can see a greater discriminatory power in each of these variables.

In order to enhance the signal-to-background ratio, especially in the very heavy Higgs

mass region, we therefore adopt the following additional constraints on the two $b-$jet system:

$$M_{bb} > 120 \text{ GeV}, \qquad \cos\theta_{bb} < 0.75, \qquad E_{b_1} > 120 \text{ GeV}. \qquad (39)$$

The resulting signal cross sections are shown in Fig. 3 for $\tan\beta = 1.5$ and 40. along with those of the background. The signal-to-background ratio has increased, but the background remains larger. However, notice the very little loss of signal at very large Higgs masses. In fact, the Higgs rates remain above 1 fb for $M_{H^\pm} \lesssim 800$ GeV. For a transverse momentum cut of 30 GeV throughout, the typical suppression on the signal (away from threshold) is again about a factor of 3 (see the insert in the figure), now similar to the case of the background.

To enhance the relative rates further and estimate the charged Higgs boson mass, we reconstruct the M_{bt} invariant mass by combining each of the reconstructed top quarks with each of the accompanying $b-$jets, as described in step (f), a quantity that we label $M_4(H)$. The resulting spectra are presented in the top plot of Fig. 4 for $\tan\beta = 40$ and three selected values of the $H^\pm$ mass along with the background. The signal distribution clearly shows a resonance at $M_4(H) \approx M_{H^\pm}$ sitting over a combinatorial continuum, while the background spectrum is broader and tends to concentrate at values of $M_4(H)$ below 300 GeV. One can sharpen the resonances at the cost of reducing the size of the signal by combining each of the reconstructed $t-$quarks with the harder $b-$jet, as in step (g) (the corresponding invariant mass is labeled as $M_2(H)$). The distributions that we obtain in this way are given in the bottom part of Fig. 4.

One sees from the figure that the signal-to-background ratio is (much) greater than one in the neighborhood of the resonant peaks. This is an advantage of the $4b-$tagged channel over the $3b-$tagged case considered in Ref. [14], where the backgrounds were found to exceed the signal. In contrast, the size of the Higgs cross section is smaller in our case, because of the kinematic suppression induced by requiring the detection of the fourth $b-$quark. However, with an annual luminosity of 100 fb^{-1}, expected from the high luminosity option of the LHC, and a very good b-tagging efficiency, one would obtain a clearly viable signal. To illustrate this we show the signal rates on the right-hand scale of Fig. 4, for an optimistic b-tagging factor of $\epsilon_b^4 = 0.1$, corresponding to $\epsilon_b = 56\%$. Such a high value is now considered realistic for the TeV-2 run at FNAL and can be achieved by combining the silicon vertex and the lepton tagging efficiencies [33]. It is also close to the optimistic expectation of a b-tagging efficiency of about 50% even for the high luminosity run of the LHC [32].

For the above efficiency and luminosity, one would obtain between ten and hundred Higgs events per year with signal-to-background ratios above one for $M_H^\pm$ as large as 800 GeV (for $\tan\beta = 40$), as shown in Tab. 4. This shows the predicted number of events in a window of 80 GeV centered around the Higgs resonances for both signal and background, together with the corresponding statistical factors $S/\sqrt{B}$. By looking at those rates, one would expect an accessible signal for $M_{H^\pm} \lesssim 600$ GeV in the high $\tan\beta$ region ($\gtrsim 40$). Similar results also hold for the case of low $\tan\beta$ values ($\lesssim 1.5$).

However, given the not too large rates of the surviving Higgs events, the actual size of the MSSM parameter space that can be covered strongly depends on the b-tagging efficiency, ϵ_b. For instance, changing it from 56% to 40% would result in a reduction of ϵ_b^4 by a factor of four. This corresponds to a suppression of the $S/\sqrt{B}$ rates of Tab. 4 by a factor of two. A similar effect would occur if a 30 GeV cut in transverse momenta of both missing and observable particles is enforced, as opposed to the 20 GeV value advocated here. In this case, the suppression would be somewhat smaller though, about a factor of 3 on the event rates and 1.7 on the statistical significances.

Before concluding, we would like to come back to and justify what we have mentioned in the Introduction: that the size of the backgrounds (6)–(7) is generally smaller than that of process (5) considered so far, for the b-tagging efficiencies assumed in this paper. Rather than re-running all the simulations for each of these additional final states, we have assumed the two (anti)top quarks to have already been reconstructed, with similar efficiency in each case. This way, we can compute the $2 \rightarrow 4$ cross sections (6)–(7) and apply the transverse momentum, pseudorapidity and separation cuts of Section 3 to the jet-jet system accompanying the $t\bar{t}$ pair, alongside those of eq. (39). We do so also for the case of process (5). (For all such computations we have resorted again to MadGraph [25].) By adopting $\epsilon_b = 0.56$ and assuming $\epsilon_{g,\ q \neq b} = 0.01$ to be the rejection factor against non-$b-$jets, then the rates obtained this way scale as follows:

$$\sigma(gg \rightarrow t\bar{t}b\bar{b})\ :\ \sigma(gb \rightarrow t\bar{t}gb)\ :\ \sigma(gg \rightarrow t\bar{t}gg\ +\ t\bar{t}q\bar{q})\ \approx\ 3.38\ :\ 0.56\ :\ 0.48. \tag{40}$$

Thus, the singly and doubly b-mis-tagged backgrounds are both one order of magnitude smaller than the pure $4b$-process. The same applies also to the other channel contributing to a possible double b-mis-tagging, i.e.,

$$gq \rightarrow t\bar{t}gq, \tag{41}$$

where $q \neq b$, whose production rates are in fact comparable to those of process (5) (about 25% smaller). Altogether, they would add a 40% or so contribution to the $t\bar{t}b\bar{b}$ background. Some of these backgrounds are likely to be enhanced by a larger probability of a $c-$quark jet faking a b-tag, which we have not taken into account. However, their inclusion would not change our main results, so that we have left these reactions aside for the time being.

5   Summary and conclusions

The discovery at the LHC of charged scalar particles would definitely confirm the existence of new physics beyond the SM. In this respect, a very special rôle is played by the charged Higgs bosons of 2-Higgs Doublet Models (2HDMs), as their production and decay dynamics can entirely be described at tree level by only two parameters. However, the feasibility

of their detection at the LHC has always been far from certain if the mass of the new particles is much larger than the top mass. Therefore, a high-on-the-list priority is to devise phenomenological strategies that would allow one to meet the difficult challenge of their detection at the LHC collider.

We have contributed here to this task by considering the production and decay of charged Higgs scalars of the MSSM in the channel $gg \to t\bar{b}H^- + \bar{t}bH^+ \to b\bar{b}t\bar{t} \to b\bar{b}b\bar{b}W^+W^-$, in which one $W^\pm$ decays hadronically and the other leptonically. The major feature of our analysis, as compared to others carried out in the past, is that all four $b-$quarks present in the final state are required to be recognised as such. The advantage of this procedure is that it allows one to exploit the differences existing between signal and background in the kinematics of the heavy quark jets. In fact, in the dominant background, $gg \to t\bar{t}b\bar{b}$, the two $b-$quarks produced in association with the $t\bar{t}$ pair are soft, collinear and at rather low invariant mass. In contrast, in the Higgs signal, at least one of the two is expected to be energetic and isolated, as long as $M_{H^\pm}$ is significantly larger than m_t. The disadvantage is that the additional $b-$quark produced in Higgs events has rather low transverse momentum, so that its detection imposes a sizeable loss of signal.

By exploiting a selection procedure that allows one to reconstruct both top and antitop masses and after imposing tight constraints on the two $b-$quarks accompanying the $t\bar{t}$ pair, we do see Higgs peaks appearing on top of a flat combinatorial background and also above the continuum from $t\bar{t}b\bar{b}$ events. Their statistical significance is such that viable signals can be obtained for charged Higgs boson masses up to 600 GeV or so, when $\tan\beta$ is either below 1.5 or above 40, with a total number of Higgs events of the order of a several tens every 100 inverse femtobarns of luminosity.

Such mass coverage is significantly higher than that achieved in previous analyses based on a triple b-tagging. However, we should stress that these conclusions rely on a high, though not unrealistic, b-tagging efficiency, of about 50% per single $b-$jet, and a transverse momentum cut on jets and leptons, of 20 GeV, somewhat lower than the threshold normally considered. If such performances can be achieved by the LHC detectors while the machine is running at high luminosity, then the 'lepton plus $4b$' channel represents a profitable new means to access such elusive yet crucial particles over significant portions of the MSSM parameter space. Besides, this channel will be very useful for the measurement of the charged Higgs boson parameters, given the higher purity of the signal in this case. Certainly, our results are sufficiently optimistic to justify a more detailed detector-level study, incorporating hadronisation of the final state partons, the effects of jet identification and reconstruction as well as a full background simulation.

17

Acknowledgements

References

[1] J.F. Gunion, H.E. Haber, G.L. Kane and S. Dawson, "The Higgs Hunters' Guide" (Addison-Wesley, Reading, MA, 1990).

[2] ALEPH Collaboration: R. Barate et al., preprint CERN/EP-99-011; L3 Collaboration: M. Acciarri et al., Phys. Lett. B446 (1999) 368.

[3] ALEPH Collaboration: R. Barate et al., Phys. Lett. B440 (1998) 419.

[4] M. Drees, E. Ma, P.N. Pandita, D.P. Roy and S.K. Vempati, Phys. Lett. B433 (1998) 346.

[5] V. Barger, M.S. Berger and P. Ohmann, Phys. Rev. D47 (1993) 1093.

[6] S. Moretti and W.J. Stirling, Phys. Lett. B347 (1995) 291; Erratum, ibidem B366 (1996) 451; A. Djouadi, J. Kalinowski and P.M. Zerwas, Z. Phys. C70 (1996) 435; E. Ma, D.P. Roy and J. Wudka, Phys. Rev. Lett. 80 (1998) 1162.

[7] CDF Collaboration: F. Abe et al., Phys. Rev. Lett. 79 (1997) 357; M. Guchait and D.P. Roy, Phys. Rev. D55 (1997) 7263; E. Keith, E. Ma and D.P. Roy, Phys. Rev. D56 (1997) 5306.

[8] B.K. Bullock, K. Hagiwara and A.D. Martin, Nucl. Phys. B395 (1993) 499.

[9] S. Raychaudhuri and D.P. Roy, Phys. Rev. D52 (1995) 1556; D53 (1996) 4902.

[10] CMS Technical Proposal, CERN/LHCC/94-38 (1994); ATLAS Technical Proposal, CERN/LHCC/94-43 (1994).

[11] K. Odagiri, Phys. Lett. B452 (1999) 327.

[12] K. Odagiri, preprint RAL-TR-1999-012, January 1999, `hep-ph/9901432`; D.P. Roy, preprint CERN/TH/99-136, May 1999, `hep-ph/9905542`.

[13] S. Moretti and K. Odagiri, in preparation.

[14] V. Barger, R.J.N. Phillips and D.P. Roy, Phys. Lett. B324 (1994) 236.

[15] J.F. Gunion, Phys. Lett. B322 (1994) 125.

[16] A.A. Barrientos Bendezú and B.A. Kniehl, Phys. Rev. D59 (1999) 015009.

[17] S. Moretti and K. Odagiri, Phys. Rev. D59 (1999) 055008.

[18] S. Moretti and K. Odagiri, Phys. Rev. D55 (1997) 5627.

[19] J.L. Diaz-Cruz and O.A. Sampayo, Phys. Rev. D50 (1994) 6820.

[20] R. Kleiss and W.J. Stirling, Nucl. Phys. B262 (1985) 235.

[21] F.A. Berends, P.H. Daverveldt and R. Kleiss, Nucl. Phys. B253 (1985) 441.

[22] C. Mana and M. Martinez, Nucl. Phys. B287 (1987) 601.

[23] S. Moretti, Phys. Rev. D50 (1994) 2016.

[24] E. Murayama, I. Watanabe and K. Hagiwara, HELAS: HELicity Amplitude Subroutines for Feynman Diagram Evaluations, KEK Report 91-11, January 1992.

[25] T. Stelzer and W.F. Long, Comp. Phys. Comm. 81 (1994) 357.

[26] G.P. Lepage, Jour. Comp. Phys. 27 (1978) 192.

[27] R. Kleiss, W.J. Stirling and S.D. Ellis, Comput. Phys. Commun. 40 (1986) 359.

[28] A.D. Martin, R.G. Roberts, W.J. Stirling and R.S. Thorne, Phys. Lett. B443 (1998) 301.

[29] M. Spira, preprint DESY 98-159, October 1998, `hep-ph/9810289`; D. Dicus, T. Stelzer, Z. Sullivan and S. Willenbrock, Phys. Rev. D59 (1999) 094016; F. Borzumati, J.-L. Kneur and N. Polonsky, preprint CERN-TH/99-118, PM/98-38, RU/98-45, August 1999, `hep-ph/9905443`.

[30] A. Djouadi, J. Kalinowski and M. Spira, Comp. Phys. Comm. 108 (1998) 56.

[31] J.A. Coarasa, D. Garcia, J. Guasch, R.A. Jiménez and J. Solà, Phys. Lett. B425 (1998) 329.

[32] E. Richter-Was and M. Sapinski (ATLAS Collaboration), internal note ATL-PHYS-98-132; V. Drollinger, T. Muller and R. Kinnunen (CMS Collaboration), internal note CMS NOTE 1999/001.

[33] G.P. Yeh, private communication.

Signal, $\tan\beta = 30$ (fb)					
$M_{A(H^\pm)}$	05A	09A	10A	01A	07A
200(214)	217.14 ± 0.18	226.67 ± 0.20	199.11 ± 0.15	204.48 ± 0.17	222.79 ± 0.18
300(310)	123.20 ± 0.10	130.79 ± 0.11	110.90 ± 0.086	116.42 ± 0.10	125.76 ± 0.11
400(407)	60.414 ± 0.059	65.256 ± 0.066	53.410 ± 0.049	57.333 ± 0.057	61.360 ± 0.059
500(506)	30.802 ± 0.044	33.895 ± 0.047	26.742 ± 0.040	29.481 ± 0.043	31.252 ± 0.045
600(605)	16.341 ± 0.029	18.268 ± 0.032	13.977 ± 0.026	15.670 ± 0.029	16.455 ± 0.029
Background (fb)					
	05A	09A	10A	01A	07A
	1863 ± 56	1949 ± 59	1706 ± 51	1755 ± 53	1901 ± 57
MRS-LO [$Q = \mu = \sqrt{\hat{s}}$]					
$4b\ +\ 2$ jets $+\ \ell^\pm\ +\ p^T_{\mathrm{miss}}$					No cuts

Table 3: Production cross section for the signal (4) (and its charge conjugate) in the decay channel (31) (top), for $\tan\beta = 30$ and five values of $M_{A(H^\pm)}$ (given in GeV) in the heavy mass range, as obtained by using five different sets of PDFs. Corresponding rates for the background (5) yielding the same signature (31) are also given. No cuts have been implemented. The renormalisation and factorisation scales are set equal to the partonic CM energy. Errors are as given by `VEGAS`.

Number of events per year			
$M_{H^\pm} \pm 40$ GeV	S	B	$S/\sqrt{\overline{B}}$
310	127.80	105.14	12.46
	57.80	41.90	8.92
407	88.56	67.63	10.76
	53.78	39.21	8.58
506	51.46	38.74	8.26
	36.32	26.86	7.00
605	29.43	21.49	6.34
	22.70	16.58	5.57
704	17.09	11.98	4.93
	14.02	9.89	4.45
803	10.03	6.75	3.86
	8.61	5.81	3.57
MRS-LO [$Q = \mu = \sqrt{\hat{s}}$]			
$4b\ +\ 2$ jets $+\ \ell^{\pm}\ +\ p_{\mathrm{miss}}^{T}$			After all cuts

Table 4: Number of events from signal (4) (and its charge conjugate) (S) and background (5) (B) in the decay channel (31), along with the statistical significance ($S/\sqrt{B}$), per 100 inverse femtobarns of integrated luminosity, in a window of 80 GeV around a few selected values of $M_{H^\pm}$ (given in GeV) in the heavy mass range, with $\tan\beta = 40$. Four $b-$jets are assumed to be tagged with overall efficiency $\epsilon_b^4 = 0.1$, i.e., $\epsilon_b = 56\%$. All cuts discussed in the text, (32)–(35), (a)–(d) and (39), have been implemented. The renormalisation and factorisation scales are set equal to the partonic CM energy. The first row corresponds to the $M_4(H)$ distribution whereas the second refers to the $M_2(H)$ one (see Fig. 4).
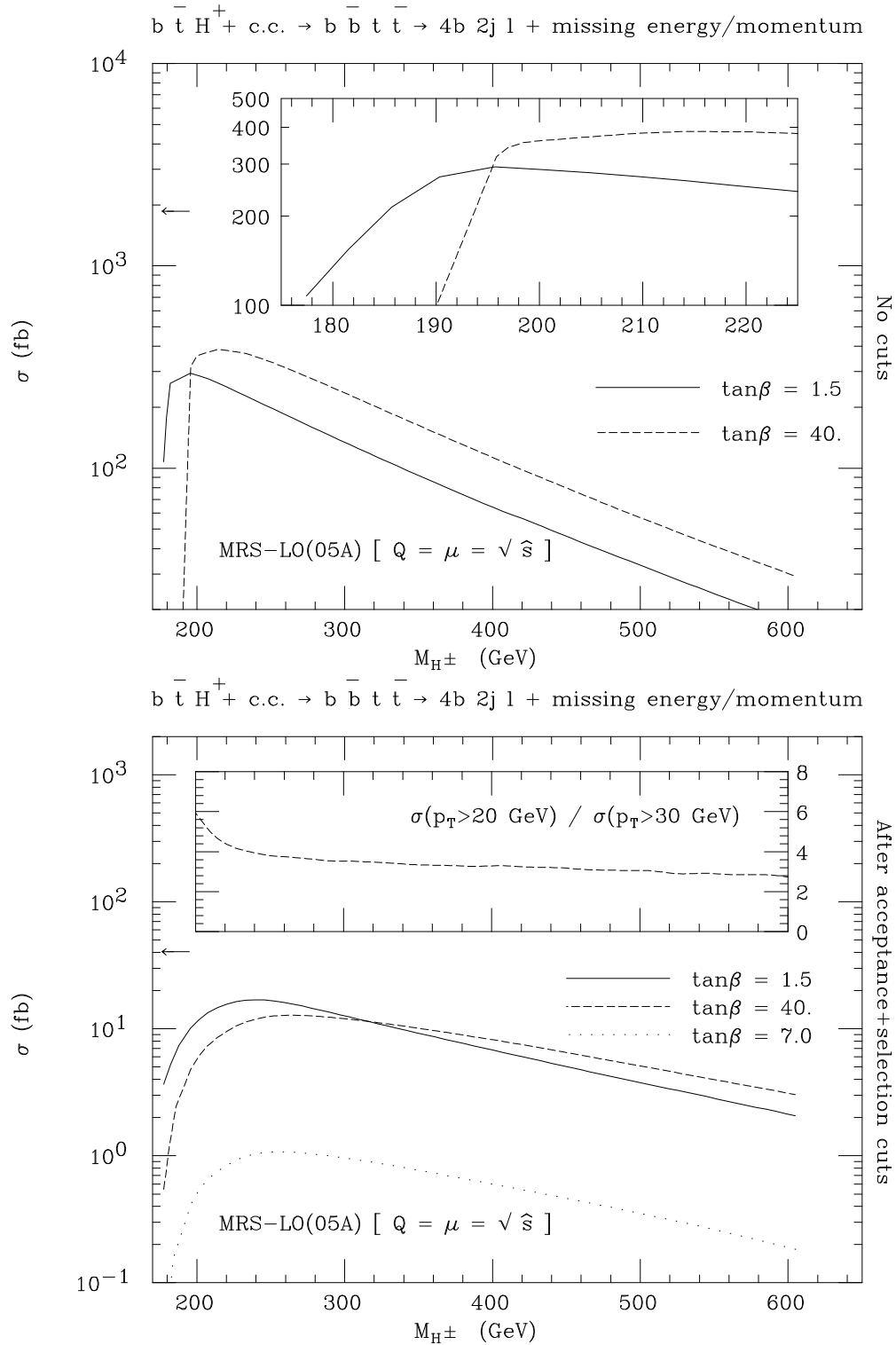
Figure 1: Production cross section for process (4) (and its charge conjugate) in the decay channel (31) as a function of $M_{H^\pm}$ in the heavy mass range, for some discrete values of $\tan\beta$, for the case in which no (upper figure) and acceptance plus selection (lower figure) cuts have been implemented. In the insert of the upper plot, we enlarge the rates in the vicinity of $M_{H^\pm} = m_t$. In the insert of the lower plot, we present the ratio between the above signal cross section for $\tan\beta = 40$ and the corresponding one obtained by adopting a threshold of 30 GeV in (32)–(33). The PDF set used was MRS-LO(05A) with renormalisation and factorisation scales set equal to the partonic CM energy. The arrow represents the size of the background (5) yielding the same signature (31). No b-tagging efficiency is included.
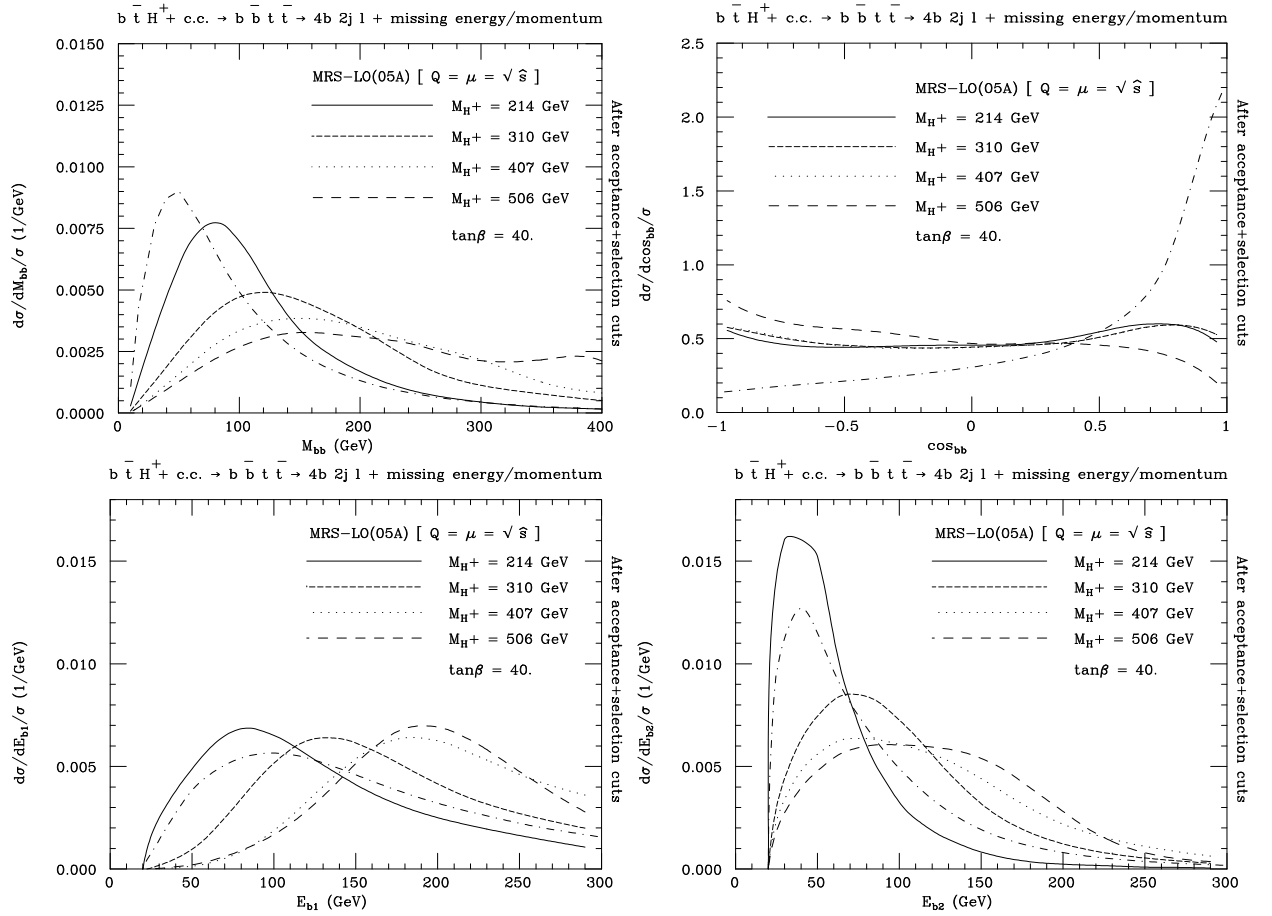
Figure 2: Differential distributions in invariant mass (top-left), in cosine of the relative angle (top-right) and in energy of the most (bottom-left) and least (bottom-right) energetic of the two b quarks accompanying the $t\bar{t}$ pair, for process (4) (and its charge conjugate) in the decay channel (31), for four selected values of $M_{H^\pm}$ in the heavy mass range, with $\tan\beta = 40$. Acceptance and selection cuts have been implemented here. The PDF set used was MRS-LO(05A) with renormalisation and factorisation scales set equal to the partonic CM energy. The fifth (dot-dashed) curve represents the shape of the background (5) yielding the same signature (31). All distributions are normalised to unity. No b-tagging efficiency is included.
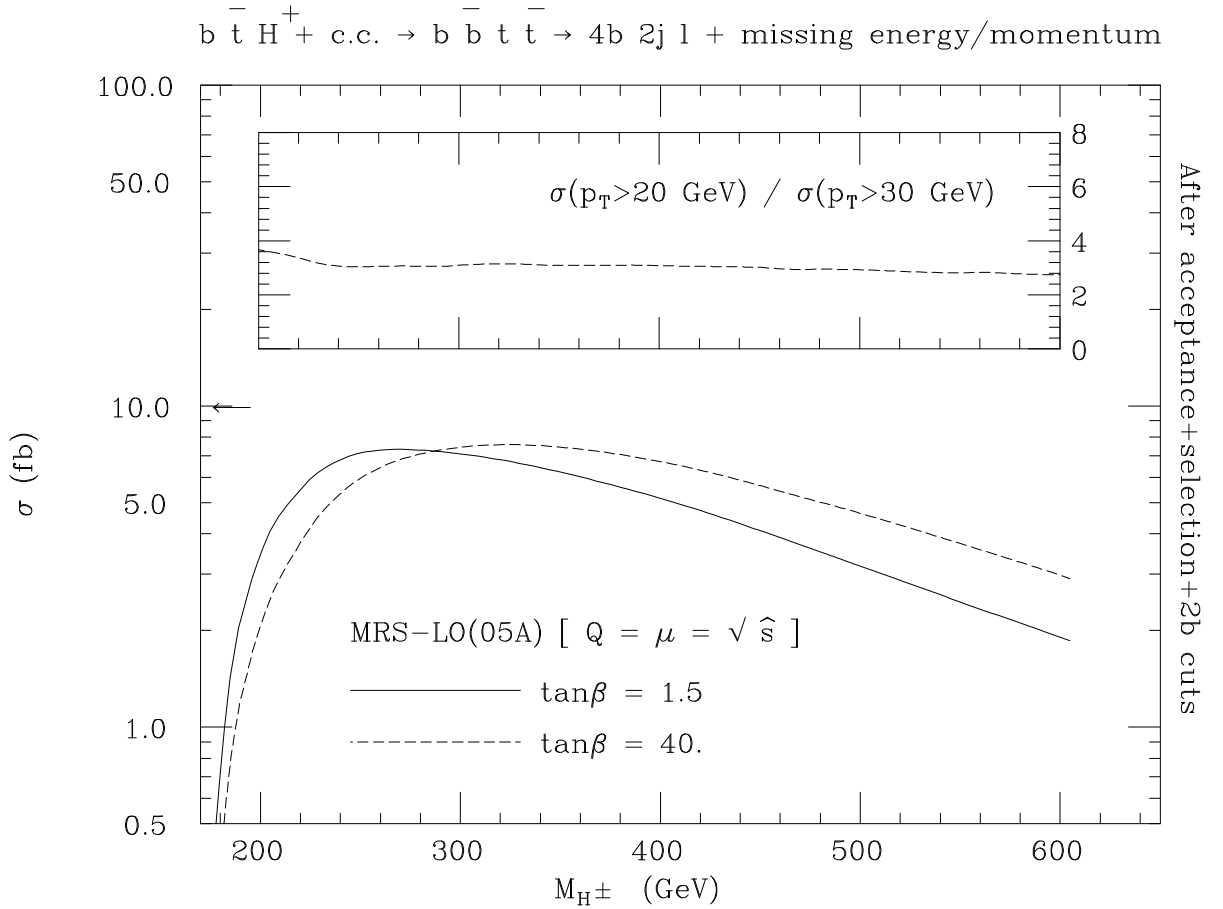
Figure 3: Production cross section for process (4) (and its charge conjugate) in the decay channel (31) as a function of $M_{H^\pm}$ in the heavy mass range, for two discrete values of $\tan\beta$. Acceptance and selection cuts have been implemented here, along with the additional cuts (39) on the $2b-$system accompanying the $t\bar{t}$ pair. In the insert, we present the ratio between the above signal cross section for $\tan\beta = 40$ and the corresponding one obtained by adopting a threshold of 30 GeV in (32)–(33). The PDF set used was MRS-LO(05A) with renormalisation and factorisation scales set equal to the partonic CM energy. The arrow represents the size of the background (5) yielding the same signature (31). No b-tagging efficiency is included.
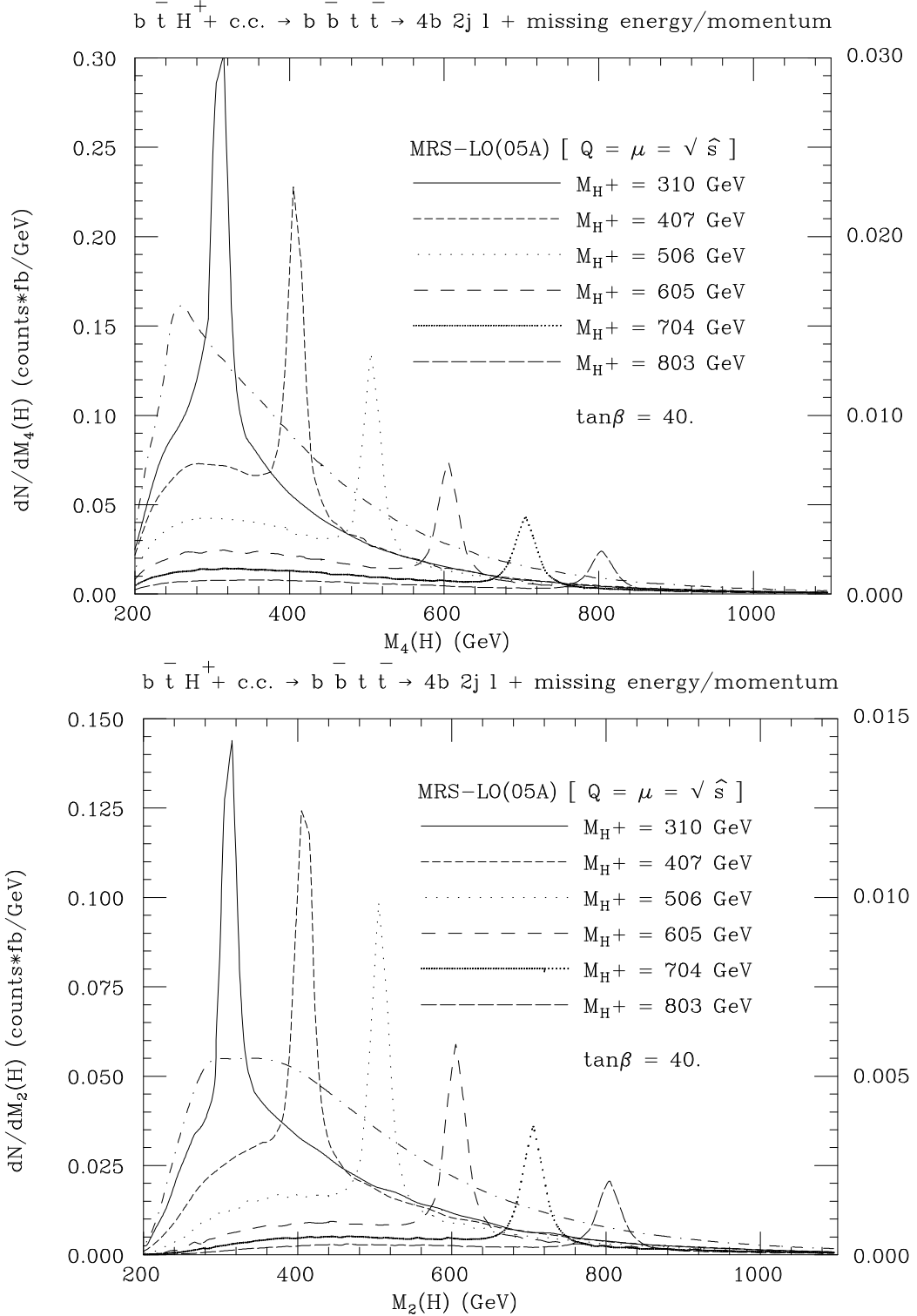
Figure 4: Differential distributions in the reconstructed charged Higgs mass for process (4) (and its charge conjugate) in the decay channel (31) for six selected values of $M_{H^\pm}$ in the heavy mass range, for $\tan\beta = 40$. Acceptance and selection cuts have been implemented here, along with the additional cuts (39) on the $2b-$system accompanying the $t\bar{t}$ pair. The PDF set used was MRS-LO(05A) with renormalisation and factorisation scales set equal to the partonic CM energy. The seventh (dot-dashed) curve represents the shape of the background (5) yielding the same signature (31). Normalisation is to the total cross sections times the number of possible '2 b + 2 jet mass' combinations: four (top) and two (bottom). The right-hand scale corresponds to a b-tagging efficiency factor of $\epsilon_b^4 = 0.1$, i.e., $\epsilon_b = 56\%$